

Article

Thermal Modeling Approaches for a LiCoO₂ Lithium-ion Battery—A Comparative Study with Experimental Validation

Edwin Paccha-Herrera ^{1,*}, Williams R. Calderón-Muñoz ^{1,2}, Marcos Orchard ^{2,3}, Francisco Jaramillo ³ and Kamal Medjaher ⁴

¹ Department of Mechanical Engineering, Faculty of Physical and Mathematical Sciences, Universidad de Chile, Beauchef 851, Santiago 8370456, Chile; wicalder@uchile.cl

² Energy Center, Universidad de Chile, Tupper 2007, Santiago 8370456, Chile; morchard@ing.uchile.cl

³ Department of Electrical Engineering, Faculty of Physical and Mathematical Sciences, Universidad de Chile, Tupper 2007, Santiago 8370456, Chile; francisco.jaramillo@ing.uchile.cl

⁴ École Nationale d'Ingénieurs de Tarbes, LGP, 47 Avenue d'Azereix, 65016 Tarbes, France; kamal.medjaher@enit.fr

* Correspondence: epaccha@ing.uchile.cl

Received: 29 June 2020; Accepted: 24 July 2020; Published: 1 August 2020



Abstract: Temperature prediction of a battery plays a significant role in terms of energy efficiency and safety of electric vehicles, as well as several kinds of electric and electronic devices. In this regard, it is crucial to identify an adequate model to study the thermal behavior of a battery. This article reports a comparative study on thermal modeling approaches by using a LiCoO₂ 26650 lithium-ion battery, and provides a methodology to characterize electrothermal phenomena. Three approaches have been implemented numerically—a thermal lumped model, a 3D computational fluid dynamics model, and an electrochemical model based on Newman, Tiedemann, Gu and Kim formulation. The last two methods were solved using ANSYS Fluent software. Simulations were validated with experimental measurements of the cell surface temperature at constant current discharge and under a highway driving cycle. Results show that the three models are consistent with actual temperature measurements. The electrochemical method has the lower error at 0.5C. Nevertheless, this model provides the higher error (1.3 °C) at 1.5C, where the maximum temperature increase of the cell was 18.1 °C. Under the driving cycle, all the models are in the same order of error. Lumped model is suitable to simulate a wide range of battery operating conditions. Furthermore, this work was expanded to study heat generation, voltage and heat transfer coefficient under natural convection.

Keywords: lithium-ion battery; MSMD; lumped model; ANSYS; natural convection; thermal management

1. Introduction

The use of electric vehicles (EVs) is becoming increasingly relevant to reduce oil consumption and avoid environmental pollution. Nevertheless, the primary challenge for clean energy vehicles is to improve the performance of their energy storage system, typically comprised of lithium-ion (Li-ion) batteries. A weak point of Li-ion batteries (LIBs) is that their behavior is strongly dependent on temperature, which advisable range of operation is between 15 °C and 35 °C [1]. Exploring the performance of the models for LIBs has potential utilization in several fields such as: condition monitoring, health assessment, remaining useful life (RUL) prediction and battery thermal management systems (BTMS).

In order to estimate the temperature of a LIB, there exist some models such as: thermal, electrochemical, equivalent circuit model (ECM) or a combination among them. A thermal model can be a lumped, one-dimensional (1D), two-dimensional (2D), or three-dimensional (3D) system, where the main input requirements for modeling are thermal properties and the heat generation rate of the battery.

Regarding the thermal lumped model, it can simulate the whole cell at a uniform temperature taking into consideration that the gradient temperature within the battery is negligible [2], and is also capable to estimate the center and surface temperature of the cell considering an internal thermal resistance [3] and the degradation of a battery pack [4]. Moreover, there exists many other thermal studies based on a lumped system. For instance, Bryden et al. [1] determined the heat capacity of many cells, Coman et al. [5] studied thermal abuse conditions, Lin et al. [6] formulated an electro-thermal model for a battery, and Gao et al. [7] proposed a reduced order model to control a battery pack. Most of the aforementioned studies on lumped models were developed employing small size batteries such as 18650 (18 mm diameter and 65 mm height) and 26650 (26 mm diameter and 65 mm height). For large format batteries, it is appropriate to study the cooling parameters to maintain a maximum temperature and uniformity of the cell [8] since the temperature gradient is considerable. For instance, in Reference [9], the authors reported the non-uniform temperature distribution for a 20 Ah LIB at discharging rates of 2C, 3C, and 4C. C-rate is the measurement of the charging or discharging current with respect to the rated capacity, for example, for a 1 Ah battery, 1C rate represents the current that completely discharges the battery in one hour.

Samba et al. [10] studied the thermal distribution for a pouch battery using a 2D computational fluid dynamics (CFD) model. Besides, some studies have employed analytical techniques such as polynomial approximation in order to estimate the heat conduction inside the battery for 1D and 2D models [11,12].

Three-dimensional thermal model is generally based on CFD solvers, and has been widely utilized by researchers to study the thermal performance of a single cell [13] and battery packs such as the work developed in References [14–16].

On the other hand, electrochemical models can be solved using multi-scale multi-domain (MSMD) approach by using electrochemical equations according to the physics of Li-ion transport in the battery at different domains and different scales [17]. This approach is useful to determine not only the temperature profile, but also relevant characteristics such as: heat generation, voltage, current flow field, and so forth. MSMD approach is implemented into Commercial software ANSYS Fluent through three sub-models: an equivalent circuit model (ECM) [18], a full electrochemical model based on Newman Pseudo-2D equations [19], and a Newman, Tiedemann, Gu and Kim (NTGK) model, which is a semi-empirical electrochemical model that requires discharging tests as input data [20]. When using NTGK model, the differences between simulated and measured cell temperatures could be less than 1 °C [21]. Furthermore, MSMD model is capable to simulate a battery pack with the cells connected electrically [22,23] and thermal runaway [24,25]. Panchal et al. [19] applied MSMD framework by solving a Newman model to determine the temperature and voltage of a 26650 LFP lithium-ion battery discharged at constant discharge rates, whereas G. Li and S. Li [17] simulated a prismatic battery under a driving cycle by the same approach.

The aforementioned models have been studied independently. For instance, Xu et al. [26] presented a comparative study oriented to thermal control for cylindrical LIBs without considering electrochemical and CDF models. A suitable thermal management system is a priority for optimal performance and safety of the batteries [27]. In particular, comparisons between an electrochemical model and the other approaches are very scarce. The main contributions of this paper are:

- To provide a methodology to characterize the electrothermal behavior of LIBs studying the heat transfer coefficients under free convection including thermal radiation effects, heat generation, and the estimation of thermal parameters.

- To compare the main approaches used for thermal modeling of a cylindrical LIB with experimental validation for a same case study.

A 26650 lithium cobalt oxide (LCO) battery was used. Three of the most employed models to study the thermal behavior of LIBs were solved numerically: a lumped model, a 3D-CFD model, and an electrochemical approach using the NTGK model. Furthermore, voltage was simulated using NTGK formulation. All of these simulations were done at the same physical conditions of the experimental tests, at constant current discharge rate, and under the highway fuel economy test (HWFET) driving cycle. Moreover, a real driving-cycle of a Nissan Leaf was studied using the lumped model.

This article is organized as follows: Section 2 presents a theoretical framework on the methods for battery modeling utilized in this work. Section 3 describes the procedure to estimate thermal parameters and heat generation rate. Comparison among the models is provided in Section 4. Conclusions are given in Section 5.

2. Theoretical Background

2.1. Battery Geometry and Meshing

Some geometry considerations are necessary to take into account depending on the model applied. The lumped model is formulated without solving spacial temperatures, except for the cell surface, where the temperature is uniform. The battery geometry employed to solve the 3D-CFD model is a solid cylinder 65 mm length and 26 mm diameter. The cell geometry for the NTGK model has three components: anode (negative tab), cathode (positive tab), and jelly-roll, as shown in Figure 1a. A detail of the jelly-roll is provided in Figure 1b. Thermal resistance through the shell is considered negligible, then it is not modeled. Also, the thermal effect due to battery holder is not studied.

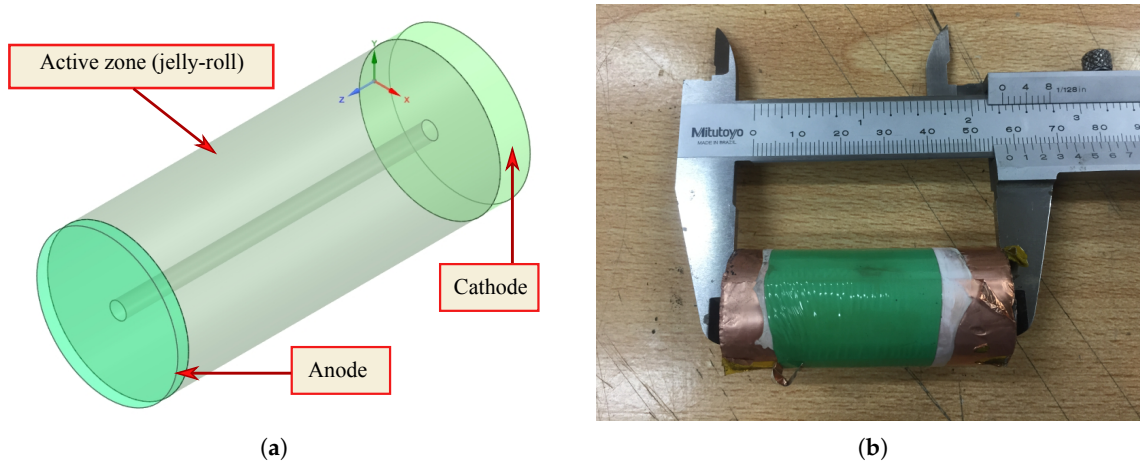


Figure 1. Battery details for Newman, Tiedemann, Gu and Kim (NTGK) model: (a) Cell geometry. (b) Jelly-roll of the lithium cobalt oxide (LCO) 26650 cell.

A mesh independence study was carried out to solve the 3D-CDF (Table 1), and NTGK model (Table 2), both modeled with a discharge current of 6 A. In each case, mesh 2 was selected taking into account that maximum temperature and total heat transfer rate do not vary when number of mesh elements is increased. In this way, a mesh with 45604 elements was selected for 3D-CFD model, and a mesh with 38777 elements was chosen for NTGK model.

Table 1. Mesh independence test for 3D-computational fluid dynamics (CFD) model.

Description	Mesh 1	Mesh 2	Mesh 3
Number of elements	1104	45604	161124
Maximum temperature (°C)	41.30	41.42	41.43
Total heat transfer rate (W)	1.51	1.52	1.52

Table 2. Mesh independence test for multi-scale multi-domain (MSMD) model.

Description	Mesh 1	Mesh 2	Mesh 3
Number of elements	1812	38777	132892
Maximum temperature (°C)	39.23	39.10	39.10
Total heat transfer rate (W)	1.31	1.31	1.31

2.2. Battery Modeling

This section exposes the thermal models solved in the present study.

2.2.1. 3D-CFD Model

The energy equation employed by CFD solver to model the battery as a solid is governed by [20]:

$$\frac{\partial}{\partial t} (\rho h_e) + \nabla \cdot (\vec{V} \rho h_e) = \nabla \cdot (k \nabla T) + S_h, \quad (1)$$

where ρ is the density, $h_e = \int c_p dT$ is the sensible enthalpy, c_p is the specific heat, k is the thermal conductivity, T is the temperature, S_h is the volumetric source term, and the velocity \vec{V} is obtained from the motion of the fluid. In the present study, instead of solving flow equations, an experimental heat transfer coefficient was utilized.

2.2.2. Thermal Lumped Model

Energy balance for a single cell also can be written as:

$$C_p \frac{\partial T}{\partial t} = Q_{conv} + Q_{rad} + Q_{gen}, \quad (2)$$

where C_p is heat capacity, Q_{gen} is the heat generation (source term), and heat exchange rate is transferred by convection Q_{conv} and radiation Q_{rad} .

This work employs a thermal lumped model proposed by Forgez et al. [3], which simplifies Equation (2) into Equation (3):

$$\frac{dT_s}{dt} = \frac{T_{amb} - T_s}{C_p (R_{in} + R_{out})} + \frac{Q_{gen} R_{out}}{C_p (R_{in} + R_{out})}, \quad (3)$$

where T_s , and T_{amb} are the surface temperature of the battery, and ambient temperature, respectively. The heat capacity, conduction resistance in the inner of the cell R_{in} , and external resistance R_{out} between the surface of the cell and surrounding fluid; can be determined via parameter identification such as References [1,28]. An equivalent thermal circuit is illustrated in Figure 2, where Q_{gen} is represented as a source of current, and C_p allows to store energy as a capacitor. Internal cell temperature T_{in} could be computed as well.

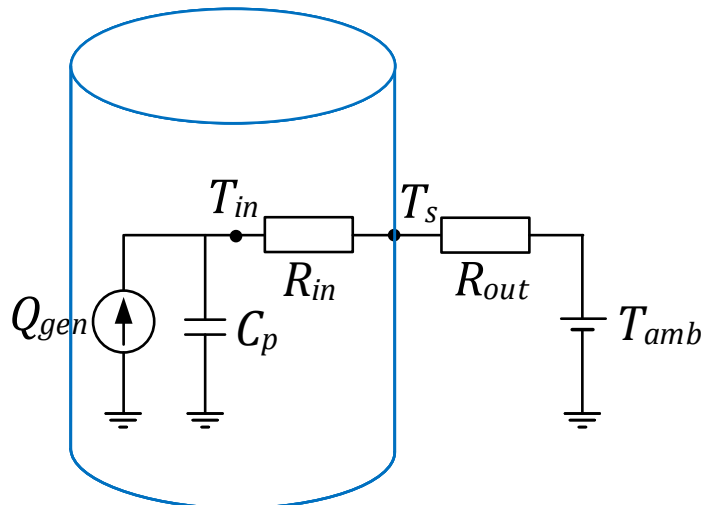


Figure 2. Simplified lumped model. Adapted from Reference [3].

2.2.3. Heat Transfer

The heat transfer rate by convection, and radiation are defined as:

$$Q_{conv} = -A_{surf,c}h_{conv}(T_s - T_{amb}) \quad (4)$$

$$Q_{rad} = -A_{surf,c}\epsilon\sigma(T_s^4 - T_{sur}^4), \quad (5)$$

where $A_{surf,c}$ is the surface area of the cell, h_{conv} is the convection heat transfer coefficient, ϵ is the emissivity of the cell surface, $\sigma = 5.67 \times 10^{-8} \text{ W m}^{-2} \text{ K}^{-4}$ is the Steffan-Boltzmann constant, and T_{sur} is the surrounding temperature for radiative heat transfer.

Considering that $T_{amb} = T_{sur}$, total heat transfer rate $Q_{ht} = Q_{conv} + Q_{rad}$ can be expressed in terms of a combined heat transfer coefficient h_{comb} as follows [29]:

$$Q_{ht} = h_{comb}A_{surf,c}(T_s - T_{amb}) \quad (6)$$

$$h_{comb} = h_{conv} + h_{rad} \quad (7)$$

$$h_{rad} = \epsilon\sigma(T_s^2 + T_{amb}^2)(T_s + T_{amb}). \quad (8)$$

Then, the following expression for R_{out} in Equation (3) can be written:

$$R_{out} = \frac{1}{h_{comb}A_{surf,c}}. \quad (9)$$

Convection coefficient h_{conv} is governed by:

$$h_{conv} = \frac{\text{Nu}_D \cdot k_f}{d}, \quad (10)$$

where k_f is the thermal conductivity of the fluid, d is the battery diameter, and Nu_D is Nusselt number computed through Equation (11), formulated by Morgan for free convection from a horizontal cylinder [29]:

$$\text{Nu}_D = C_{Nu} \cdot Ra_D^n, \quad (11)$$

where C_{Nu} and n are constants according to the Rayleigh number Ra_D .

2.2.4. Heat Generation

Bernardi et al. [30] developed the following expression to compute the heat generation inside a battery:

$$Q_{gen} = I(V_{OC} - V) - I \left(T \frac{dV_{OC}}{dT} \right) = I^2 R_T - I \left(T \frac{dV_{OC}}{dT} \right), \quad (12)$$

where the current I is positive for discharging and negative for charging. Both open circuit potential (V_{OC}) and the total internal resistance of the battery R_T depend on the state-of-charge (SOC) and temperature of the cell. The term $I(V_{OC} - V)$ of Equation (12) represents the heating due to the Joule effect (irreversible heat generation). The second term is the entropy change (reversible heat generation), attributed to electrochemical reactions [15]. Besides, phase change effect, mixing effect, and simultaneous reactions are neglected in the Bernardi's formulation.

In the present approach, the battery state-of-charge (SOC) is estimated by ampere-hour integration or Coulomb counting method [11]:

$$SOC = SOC_{t=0} - \frac{1}{C_N} \int I(t) dt, \quad (13)$$

where $SOC_{t=0} = 1$ (when the battery is 100% charged), and C_N is the nominal capacity of the cell.

Regarding the total internal resistance of a cell, the most common method to determine its value is the hybrid pulse power characterization (HPPC) test [31,32]; nonetheless, electrochemical impedance spectroscopy (EIS) can help to characterize the internal impedance of the battery, and evaluate individually all components of total resistance [33].

2.2.5. Electrochemical Impedance Spectroscopy (EIS)

EIS is a non-destructive method based on frequency analysis, which helps to characterize the internal impedance of cells at specific SOC values. A small amplitude signal, either voltage (potentiostatic) or current (galvanostatic), is applied to the battery during the test trying to minimize disturbances on the actual battery SOC. The collected data allows to identify a model for the battery, capturing the electrical dynamic response in terms of an ECM such as a lumped-parameter Thévenin Equivalent Circuit [34].

Results of EIS test are normally presented through a Nyquist plot as shown in Figure 3. Pure ohmic resistance R_o is the value at the interception of the curve and the horizontal axis. The real part of the impedance at local minimum point A corresponds to the total resistance quantified from methods such as HPPC test [33,35]. Hence, the total internal resistance of the battery is considered as the sum of ohmic resistance and charge transfer resistance R_{CT} .

2.2.6. Ntgk Model

The NTGK model based on dual potential MSMD framework computes the thermal and electric field of the battery as follows [20]:

$$\frac{\partial \rho C_p T}{\partial t} - \nabla \cdot (k_c \nabla T) = \sigma_{pos} |\nabla \phi_{pos}|^2 + \sigma_{neg} |\nabla \phi_{neg}|^2 + q_{ech} \quad (14)$$

$$\begin{aligned} \nabla \cdot (\sigma_{pos} \nabla \phi_{pos}) &= -j \\ \nabla \cdot (\sigma_{neg} \nabla \phi_{neg}) &= j, \end{aligned} \quad (15)$$

where σ is the electric conductivity, ϕ is the electric potential, and subscripts *pos* and *neg* refer to positive and negative electrode, respectively.

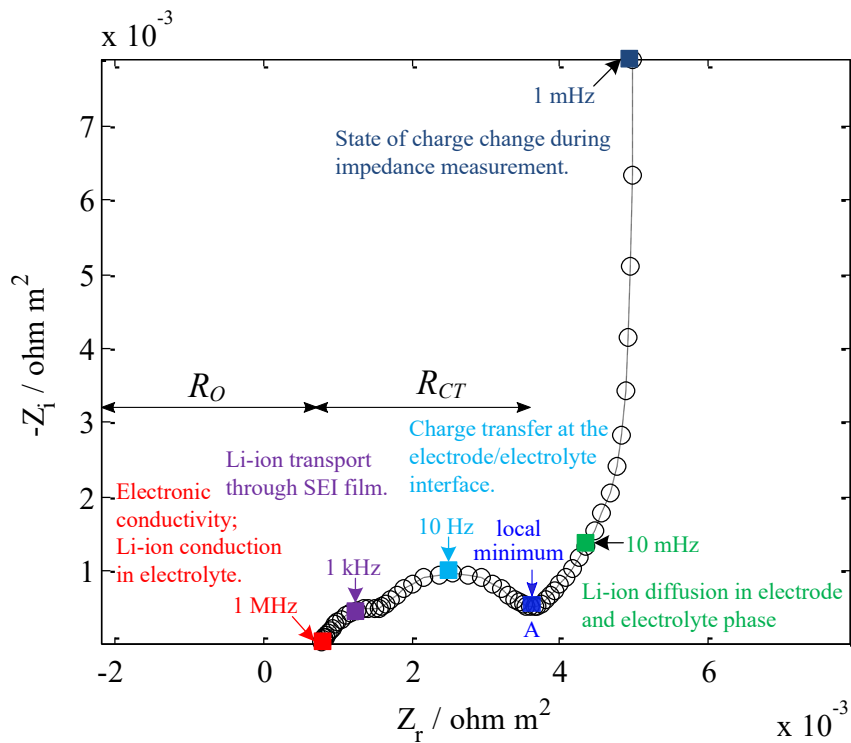


Figure 3. Nyquist plot scheme of electrochemical impedance spectroscopy (EIS). Adapted from Reference [36].

The volumetric current transfer rate j is formulated as [37]:

$$j = \frac{C_N}{C_{ref} Vol} Y [U - (\phi_{pos} - \phi_{neg})], \quad (16)$$

where Vol is the volume of active zone, C_{ref} is the capacity of the battery used to obtain the parameters of the functions U and Y (Table 3), which are determined by the Parameter Estimation Tool in Fluent by using discharging experiments. Based on the deep-of-discharge (DoD), these functions are computed as follow [37]:

$$\begin{aligned} U &= \left(\sum_{n=0}^5 a_n (DoD)^n \right) - C_2 (T - T_{ref}) \\ Y &= \left(\sum_{n=0}^5 b_n (DoD)^n \right) \exp \left[-C_1 \left(\frac{1}{T} - \frac{1}{T_{ref}} \right) \right], \end{aligned} \quad (17)$$

where C_1 and C_2 are constants for a specific battery, and T_{ref} is the reference temperature.

Table 3. Parameters for NTGK model

Functions	Coefficients					
U	a_0 4.0682	a_1 -1.2669	a_2 -0.9072	a_3 3.7550	a_4 -2.3108	a_5 -0.1701
Y	b_0 16.5066	b_1 -27.0367	b_2 237.3297	b_3 -632.603	b_4 725.0825	b_5 -309.8760

The heat due to electrochemical reactions q_{ech} is written as [20]:

$$q_{\text{ech}} = j \left[U - (\phi_{pos} - \phi_{neg}) - T \frac{dU}{dT} \right], \quad (18)$$

where the first term represents the overpotential heat, and the second term is the entropic component. Properties of the materials for NTGK model are detailed in Table 4.

Table 4. Properties of materials for MSMD model.

Property	Active Zone (jelly-roll)	Positive Tab (aluminium)	Negative Tab (steel)
Density (kg m^{-3})	2226 ^a	2719	8030
Specific heat ($\text{J kg}^{-1} \text{K}^{-1}$)	1197 ^b	871	502.48
Thermal conductivity: radial, tangential, axial ($\text{W m}^{-1} \text{K}^{-1}$)	0.8, 27, 27 [38]	202.4	16.27
Electric conductivity (Sm^{-1})	0	3.541×10^7	8.33×10^6

^a Measured. ^b Parameter estimation.

3. Materials and Methods

The contributions in this paper are as follows—firstly, to characterize the heat transfer coefficients of a battery under free convection including thermal radiation effects; secondly, to estimate the parameters; and thirdly, to compare the main approaches used for thermal modeling of a LIB with experimental validation at constant and variable current rates. Besides, heat generation and voltage are solved.

Figure 4 depicts the general procedure to develop the present study. The first step is to obtain the heat generation rate of the battery by estimating the internal resistance R_T using EIS, and the entropic coefficient applying the potentiometric method. Next stage is to estimate heat capacity and internal thermal resistance of the cell R_{in} via parameter identification. Next step is to perform battery discharging tests while ambient temperature, cell surface temperature, and heat flux from the LIB are recorded. Discharging tests allow to obtain U and Y functions using parameter estimation tool in Fluent. Finally, the models are numerically solved using MATLAB for lumped model, and ANSYS Fluent 19.2 based on finite volume method, for both 3D-CFD and NTGK models.

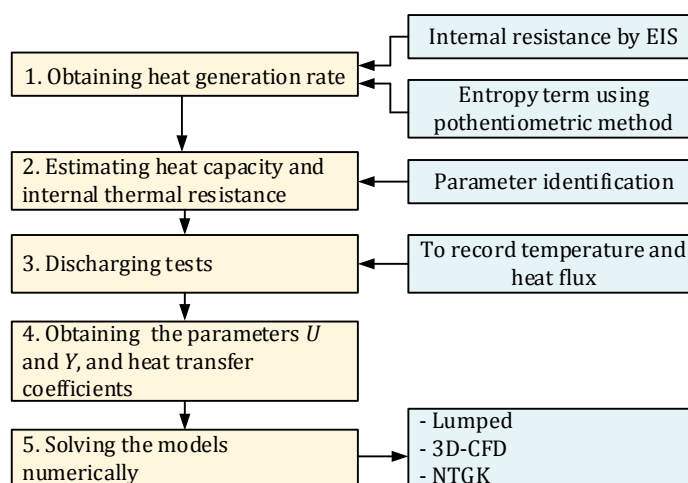


Figure 4. Methodology scheme.

3.1. Experimental Set-Up

An ICR 26650 battery (see specifications in Table 5) was fully charged following the constant-current constant-voltage (CC-CV) protocol using a battery charger (iCharger 208B). The first stage (constant-current) was at 2 A, then the charger turns to constant voltage. Subsequently, the battery was discharged using a BK Precision 8500 programmable DC load (Figure 5a). Current rates applied were 2 A (0.5C), 4 A (1C), 6 A (1.5C), and also a variable current profile. This last profile was obtained

by ADVISOR software selecting a highway HWFET-driving cycle as velocity input for an electric vehicle. The simulated current was scaled at a maximum of 5.5 A, as shown in Figure 6, and this cycle was repeatedly applied to the cell until the energy extracted was 4 Ah. Regeneration current was not considered.

Table 5. Battery specifications.

Property	Value
Diameter	26 mm
Height	65 mm
Mass (measured)	0.088 kg
Cathode material	LiCoO ₂
Anode material	Graphite
Nominal capacity	4 Ah
Tested capacity	4.3 Ah
Nominal voltage	3.7 V
Cut off voltage	2.75 V
Charge limit voltage	4.2 V
Maximum charge current	1 C
Maximum discharge current	2 C
Emissivity [5]	0.8

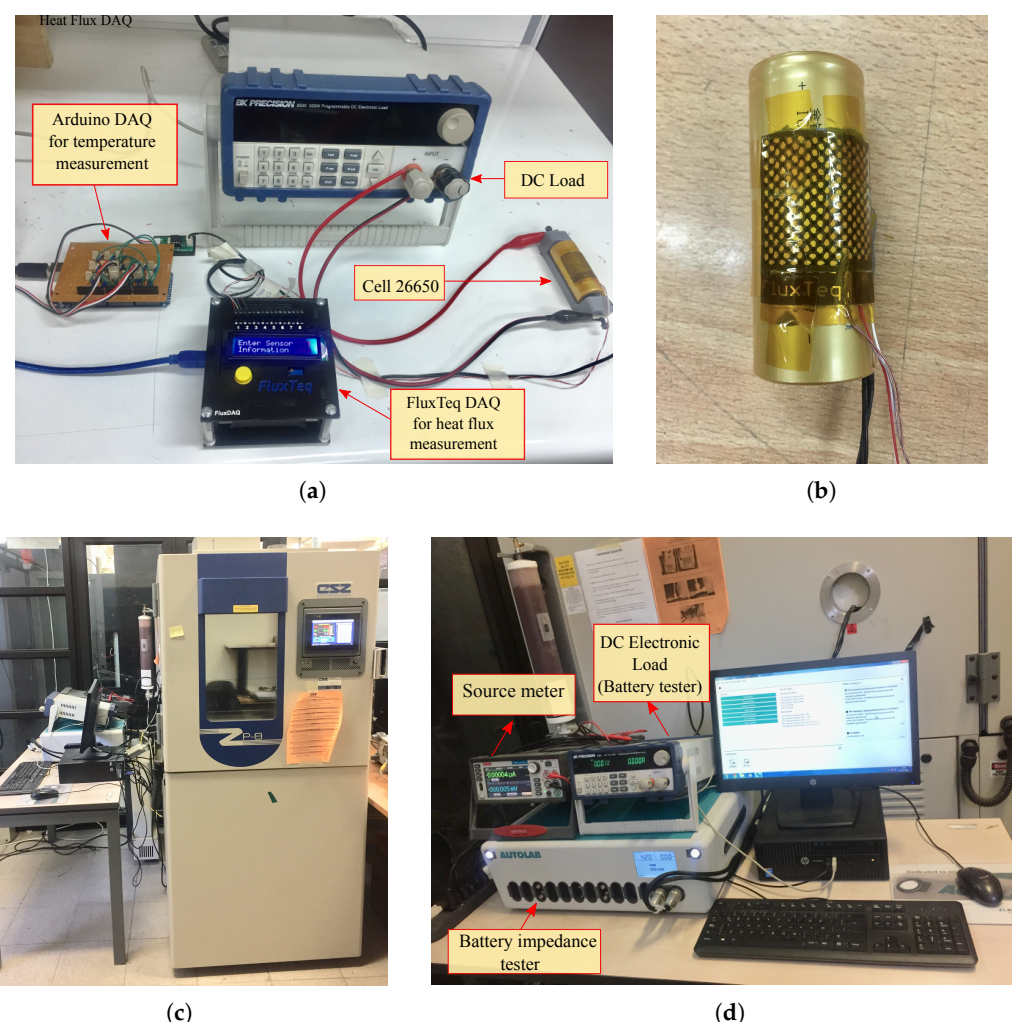


Figure 5. Experimental set-up. (a) Set-up for a discharging test. (b) Detail of the heat flux sensor. (c) Thermal chamber. (d) Equipment for EIS test.

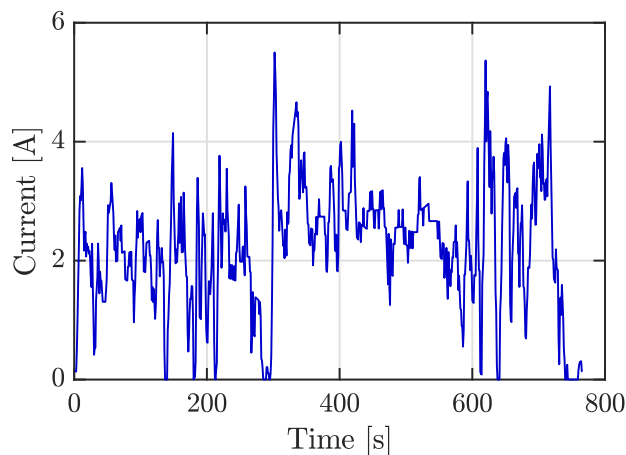


Figure 6. Scaled current profile of a highway fuel economy test (HWFET)-driving cycle.

All discharging tests were repeated five times to ensure repeatability measurements. Ambient temperature and cell temperature were recorded through a negative temperature coefficient (NTC) thermistor (ZX-Thermometer) connected to an Arduino processor board. This sensor operates between $-20\text{ }^{\circ}\text{C}$ and $85\text{ }^{\circ}\text{C}$ with an uncertainty of $\pm 0.5\text{ }^{\circ}\text{C}$. It requires a direct-current supply voltage between $+1.8\text{ V}$ and $+5.0\text{ V}$. A code was developed using MATLAB software to convert voltage input (from Arduino board) into temperature. Since ambient temperature fluctuations were less than $1\text{ }^{\circ}\text{C}$ during all tests, this value was assumed to be constant. Heat flux from the cell was measured by a PHFS-01 FluxTeq heat flux sensor (Figure 5b) connected to a FluxTeq DAQ (see Figure 5a). Measurements of heat flux are plotted in Figure 7.

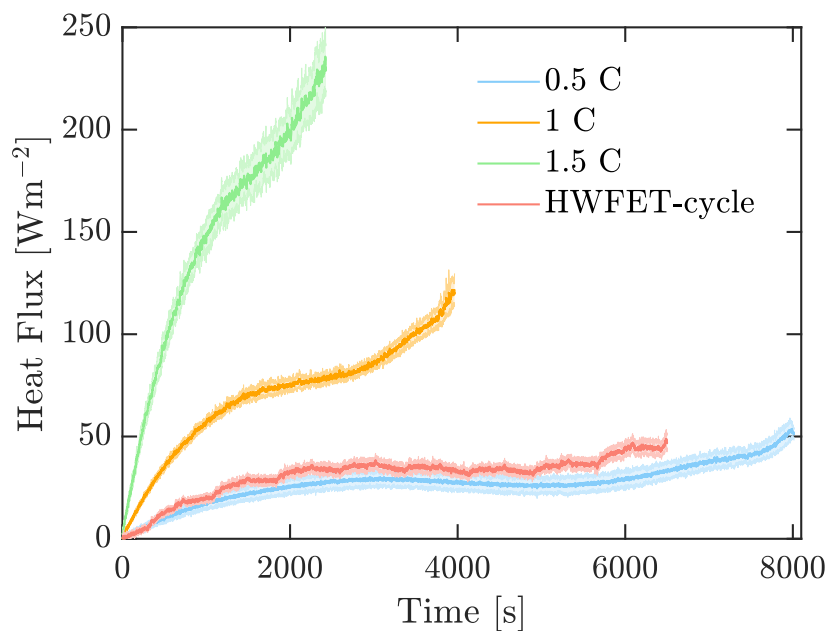


Figure 7. Measured heat flux at different discharging rates.

3.2. Heat Generation Estimation

Heat generation in the cell was computed from Equation (12) that includes internal resistance and entropy change.

3.2.1. Experiment for Internal Resistance

Electrochemical impedance spectroscopy (EIS) was carried out to estimate the internal resistance of the battery. First, the fully charged battery was placed in a thermal chamber EZT-570i (see Figure 5c) at 15 °C. After 2 hours of rest, galvanostatic EIS was conducted by using an impedance tester equipment PGSTAT302N (see Figure 5d). Details of the setup are listed in Table 6. This process was repeated at 25 °C, 35 °C, and 45 °C. After performing the experiment at 45 °C, the battery was discharged at 90% SOC and overnighted. The whole process was repeated until the cell was completely discharged (0% SOC), decreasing the battery SOC in intervals of 10% between each of the EIS tests.

Table 6. Parameters for the EIS experiment.

Parameter	Description
First applied frequency	10^4 Hz
Last applied frequency	0.005 Hz
Number of frequencies	10 per decade
Frequency step type	Points per decade
Amplitude	0.05 A
Wave type	Sine

The experimental characterization of the battery internal resistance at different temperatures, obtained from EIS tests, is depicted in Figure 8. It reveals that at lower temperature, and near to 0% of SOC, the cell resistance increases. At 35 °C and 45 °C, the resistance has practically the same value.

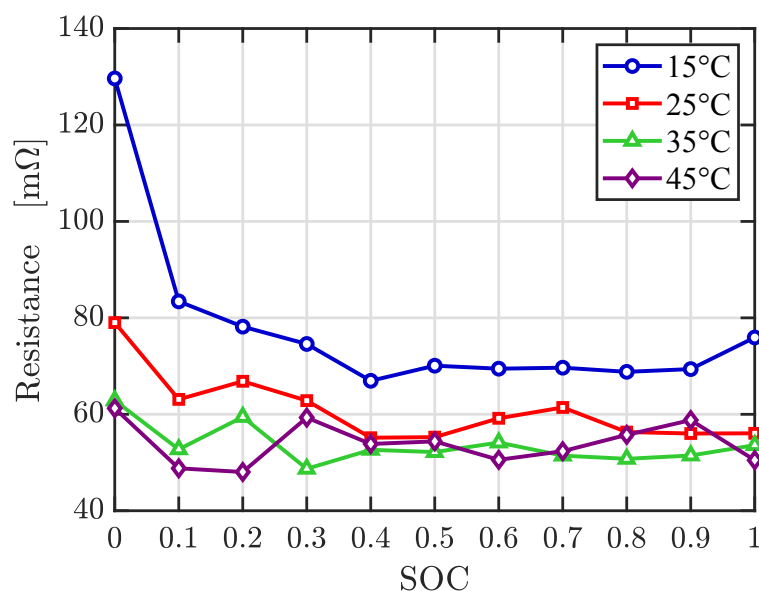


Figure 8. Internal resistance.

Average battery resistance for each discharging rate test is detailed in Table 7. It is evident that at lower discharge rates, the resistance increases. Each value represents R_T in Equation (12), that is, it allows to compute the irreversible heating.

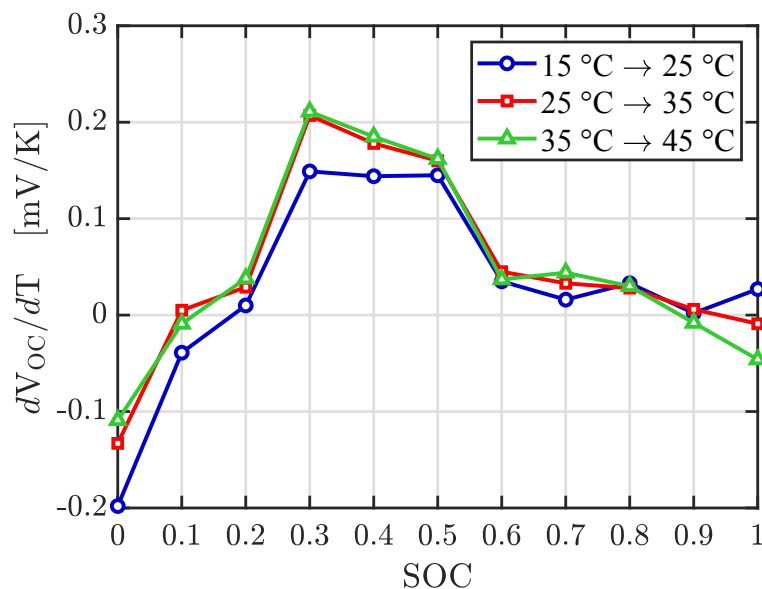
Table 7. Average cell resistance.

Current	Resistance (mΩ)	Ambient Temperature (°C)
0.5C	57.7	24
1C	55.3	24
1.5C	53.9	23
HWFET-cycle	56.8	25

3.2.2. Entropy Coefficient Experiment

Entropy change term is expressed as a relationship between open circuit voltage and cell temperature, and was obtained by applying the potentiometric method: the battery 100% charged was put into a thermal chamber at 15 °C. After it rested for two hours to reach thermal equilibrium [15], and the voltage was measured by using a KEITHLEY 2460 sourcemeter. In order to obtain the relationship dV_{OC}/dT , the same process was performed progressively at 25, 35, and 45 °C, respectively. Next, the cell was discharged at 90% SOC and overnighed. The whole test described before was repeated with intervals of 10% of SOC until the charge of the battery drops to 0% of SOC [39].

Experimental values for the entropy term are presented in Figure 9. There does not exist a significant variation of entropy change at the different temperatures. In the interval of 20% to 80%, the entropy change is positive with a maximum value near to 0.2 mV/K. A similar entropy profile was reported by Zhang et al. [40].

**Figure 9.** Entropy change coefficient.

3.3. Heat Capacity and Internal Thermal Resistance

To estimate heat capacity and internal thermal resistance, a consecutive current pulse of 0.4 A, 2 A, 4 A, and 3 A, each one of them with a duration of 10 s, was continuously applied until the battery was discharged. Ambient and battery temperatures, and heat flux were recorded as depicted in Figure 10a, and Figure 10b, respectively. These measurements allow to compute h_{comb} by least squares regression from Equation (6), and then, R_{out} from Equation (9). After obtaining h_{comb} , it is possible to figure out an experimental h_{conv} from Equation (7).

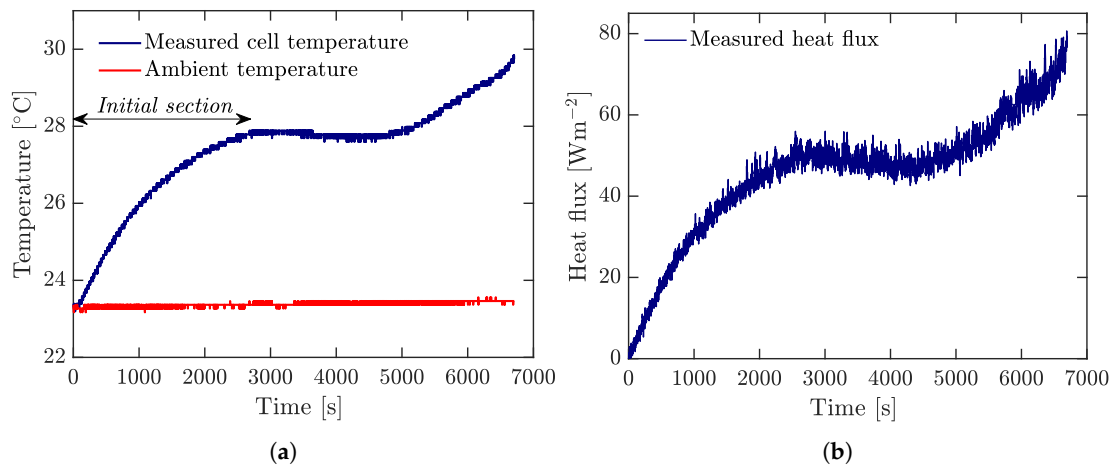


Figure 10. Measurements under applying the current pulse of 0.4 A, 2 A, 4 A, and 3 A: (a) Battery surface temperature and ambient temperature. (b) Battery heat flux.

Following a similar procedure proposed by Bryden et al. [1], the next stage was to estimate C_p and R_{in} from Equation (3) by fitting the *initial section* of the measured cell temperature (see Figure 10a), where the temperature gradient is greater. This region was taken for the first 2700 s. Parameters obtained from this section are given in Table 8. Then, specific heat is obtained by $c_p = m^{-1}C_p = 1197 \text{ Jkg}^{-1} \text{ K}^{-1}$. The aforementioned authors reported values of $R_{in} = 1.4 \text{ KW}^{-1}$ and $c_p = 1169 \text{ Jkg}^{-1} \text{ K}^{-1}$ for a 26650 LFP battery.

Table 8. Thermal parameters obtained.

$R_{out} (\text{KW}^{-1})$	$R_{in} (\text{KW}^{-1})$	$C_p (\text{JK}^{-1})$
15.8 ± 2.7	1.8 ± 0.4	105.3 ± 3.8

3.4. Physical Properties and Solving

Properties detailed in Table 9 were used to solve the lumped and 3D-CFD models. For NTGK approach, parameters and properties are given in Tables 3 and 4, respectively. Besides, for all three proposed models, there were utilized experimental heat transfer coefficients based on heat flux and temperature measurements of the cell surface. These coefficients are discussed in the Section 4.2, and were obtained following a similar procedure described in the Section 3.3. Furthermore, it was assumed that the external radiation temperature is the same as the ambient temperature.. The nominal capacity of the cell is 4 Ah; however, the average tested capacity was 4.3 Ah, and this last value was employed.

According to the current profile applied to simulate the 3D-CFD approach, there are two considerations to couple the heat generation per unit volume to the energy equation. Firstly, for constant current rates, a User Define Function (UDF) was utilized. Secondly, for variable currents (HWFET-cycle), a transient table was employed. In contrast, the NTGK model automatically computes the heat generation rate.

Numerically, the lumped model was solved by Runge Kutta Fourth order method, and the other two models were computed through a Semi-Implicit Method for Pressure Linked Equations (SIMPLE) scheme. For current rates of 2 A, 4 A, 6 A, and HWFET-cycle, the simulation time was 8015 s, 3964 s, 2430 s, and 6500 s, respectively. Furthermore, 1 s time step was utilized in all cases.

Table 9. Properties of materials for lumped and 3D-CFD models.

Property	Value	Lumped	3D-CFD
Density (kgm^{-3})	2550 ^a	✓	✓
Specific heat ($\text{Jkg}^{-1}\text{K}^{-1}$)	1197 ^b	✓	✓
Thermal conductivity: radial, tangential, axial ($\text{Wm}^{-1}\text{K}^{-1}$)	0.8, 27, 27 [38]	✗	✓
Inner thermal resistance (KW^{-1})	1.8 ^b	✓	✗

^a Computed. ^b Parameter estimation.

4. Results and Discussion

4.1. Heat Generation Rate

The behavior of the volumetric heat generation rate computed by Equation (12) and the NTGK model is depicted in Figure 11. Heat generation given by NTGK approach at constant current tends to increase, specially at the beginning and at the end of the discharge time (Figure 11a). The curves based on Bernardi's equation (dashed lines) have a concave region due to the effect of the entropic term. For HWFET driving cycle, heat generation varies according to the current profile as shown in Figure 6.

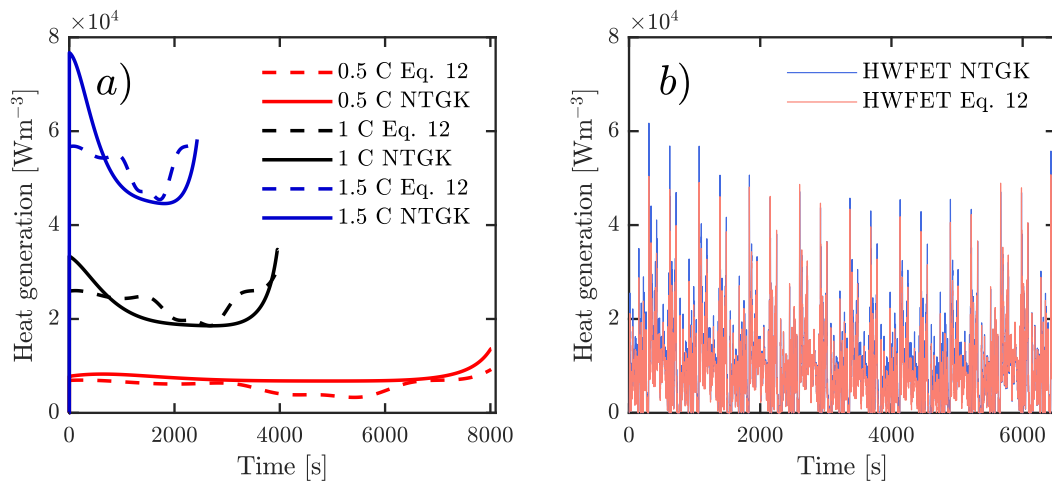


Figure 11. Volumetric battery heat generation: (a) At constant C-rate, (b) Under HWFET driving cycle.

Average of volumetric heat generation is reported in Table 10. In general, experimentally-based values (Equation (12)) are moderately close to values obtained numerically by NTGK model, but there exists a maximum percentage of variation of 30.9% at 0.5C.

Table 10. Average heat generation.

Current	Equation (12) (Wm^{-3})	NTGK Model (Wm^{-3})	Percentage of Variation (%)
0.5C	5761	7542	30.9
1C	23588	22228	5.8
1.5C	52715	52465	0.5
HWFET-cycle	8597	9861	14.7

4.2. Heat Transfer Coefficient

According to Table 11, experimental heat transfer coefficients are in moderate agreement with their computed values, although the first ones are slightly higher than predicted results. Moreover, h_{conv} is very close to a value of $5 \text{ Wm}^{-2} \text{ K}^{-1}$ used by some authors [17,24,41] for studies on LIBs performance under natural convection. Besides, it is evident from Table 11 that h_{rad} has practically the same contribution of h_{conv} in terms of heat exchange under free convection. This was also reported by Allafi et al. [42]. In general, heat transfer coefficient raises as discharge current increases.

Table 11. Convection coefficient comparison.

Current	$h_{comb} (\text{Wm}^{-2} \text{ K}^{-1})$		$h_{conv} (\text{Wm}^{-2} \text{ K}^{-1})$		$h_{rad} (\text{Wm}^{-2} \text{ K}^{-1})$
	Exp.	Computed Equations (7),(8) and (10)	Exp.	Computed Equation (10)	Equation (8)
0.5C	8.4	8.5	3.6	3.7	4.8
1C	10.2	9.2	5.3	4.3	4.9
1.5C	12.8	9.8	7.7	4.8	5.0
HWFET-cycle	8.8	8.7	3.9	3.8	4.9

4.3. Temperature Performance Comparison

All three evaluated approaches successfully estimate the cell temperature as displayed in Figure 12. The standard deviation of the experimental temperatures at each discharging test is $0.3 \text{ }^{\circ}\text{C}$, $0.2 \text{ }^{\circ}\text{C}$, $0.3 \text{ }^{\circ}\text{C}$, and $0.2 \text{ }^{\circ}\text{C}$ for 0.5C, 1C, 1.5C, and HWFET-cycle, respectively. The maximum temperature increase was $18.1 \text{ }^{\circ}\text{C}$ for 1.5C rate. Moreover, the measured temperature distribution of the cell is the same as its respective heat flux curve, as shown in Figure 7.

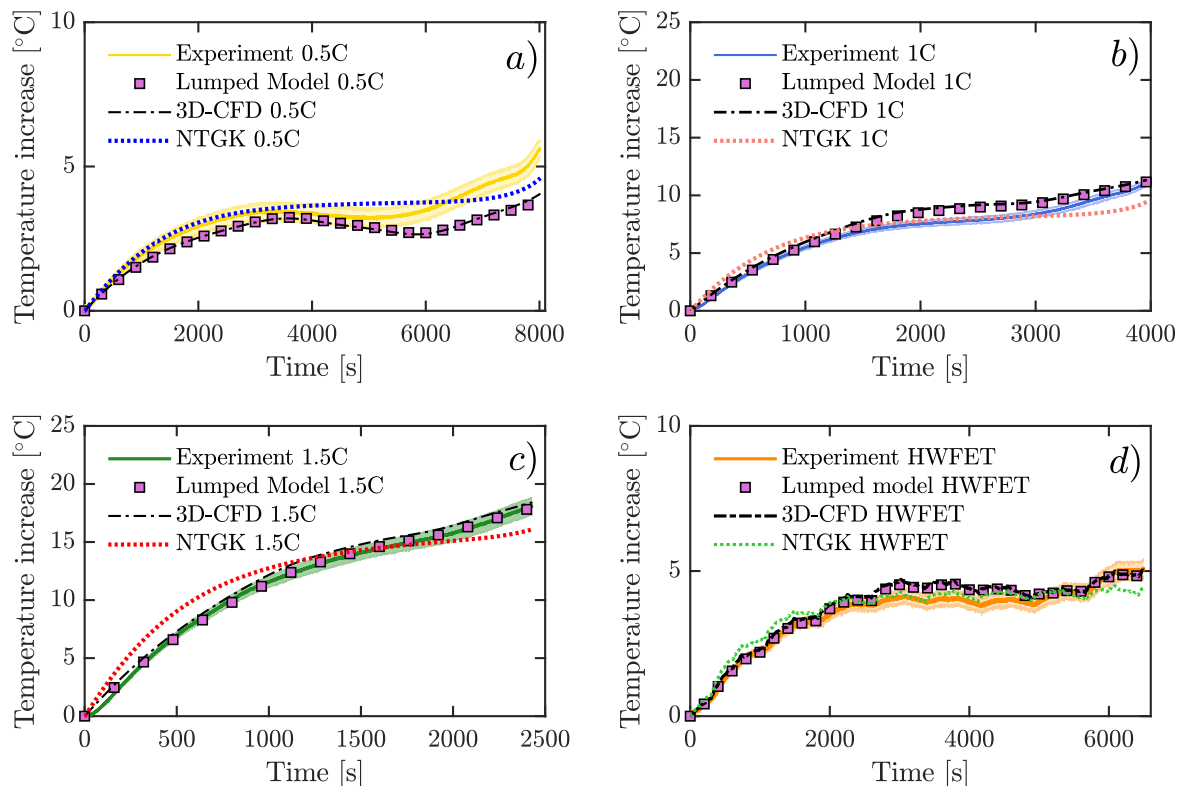


Figure 12. Comparison of temperature increase among different methods at different discharging currents: (a) 0.5C-rate. (b) 1C-rate. (c) 1.5C-rate. (d) HWFET-cycle.

All the simulated models are consistent with their experimental temperature. The lumped and 3D-CFD models have practically the same temperature distribution, it is mainly due to the heat generation term is the same for both. Nevertheless, there exist minimal discrepancies comparing the temperature profile among the proposed methods. This fact is supported by computing root mean square (RMS) errors, which are detailed in Table 12, where NTGK model has the lower error at 0.5C and 1C; however, this model has the maximum error (1.3°C) at 1.5C. For the HWFET-cycle, all models are in the same order of RMS error capturing satisfactorily the dynamics of the battery temperature under a real driving cycle (Figure 12d). In general, electrochemical models are widely used to model temperature and voltage of batteries due to their good agreement between numerical and experimental data [43], although these models require cautious attention to determine parameters such in References [44,45]. One advantage of CFD-based models is the computation of spatial temperatures, and also their flexibility to combine cells into a pack under different cooling conditions.

Table 12. Root mean square (RMS) errors for the different cases. Units $^{\circ}\text{C}$.

Current	Lumped	3D-CDF	NTGK	Experimental ΔT ($^{\circ}\text{C}$)
0.5C	0.7	0.6	0.3	5.6
1C	0.7	0.9	0.8	11.1
1.5C	0.2	0.6	1.3	18.1
HWFET-cycle	0.3	0.3	0.3	5.1

Moreover, lumped model can be more practical to evaluate long simulation time profiles. For instance, Figure 13 (bottom) shows the temperature behavior of the LCO battery considered in this study, simulated at different ambient temperatures under a real driving-cycle of a Nissan Leaf in a rural road with light traffic during approximately 5.2 h. The simulation time for each temperature distribution was 29.1 s. The application of the lumped model could be extended to estimate the temperature of a battery pack [7,46], and also battery degradation in electric vehicles [47]. Currently, the application of lumped model to estimate the temperature of an EV battery pack under different real driving cycles is being investigated. Further results will be reported in future research publications.

Besides, the models also estimate the battery temperature under forced convection. For example, Figure 14 shows a simulation of the models under the maximum discharging rate (2C) of the battery studied here considering $h_{conv} = 100 \text{ W m}^{-2} \text{ K}^{-1}$. As the discharge current increase, the temperature given by the NTGK model tends to be greater with respect to the other models at the beginning of the discharge time. This behavior mainly depends on the functions U and Y , and could be improved by adjusting the constant C_1 . Moreover, one characteristic of the ICR 26650 battery is that its tested capacity decreases to approximately 3.6 Ah when the maximum discharging current is applied.

The behavior of all the approaches can be improved. For instance, the heat capacity is the most sensitive parameter for thermal modeling while thermal conductivity has a minor impact on the simulations [13]. Then, a more accurate value of thermal parameters can be found by using calorimetric techniques. Moreover, the use of a full electrochemical model (Newman formulation) is relevant to study the physical phenomena of Li-ion transport.

4.4. Voltage

Figure 15 depicts the comparison between experimental and simulated voltage by using NTGK model. Both values are in good agreement. For HWFET driving-cycle, peak values of experimental voltage are slightly higher than the numerical result. In general terms, the dynamical behavior of the system is well captured. There exist some discrepancies specially at the end of the discharge process, where the minimal voltage is not reached; this behavior was also reported by Celik et al. [21] using NTGK model, and by Li et al. [18] using the MSMD approach under the electric circuit model. Voltage given by NTGK model could be improved by adjusting the C_2 constant.

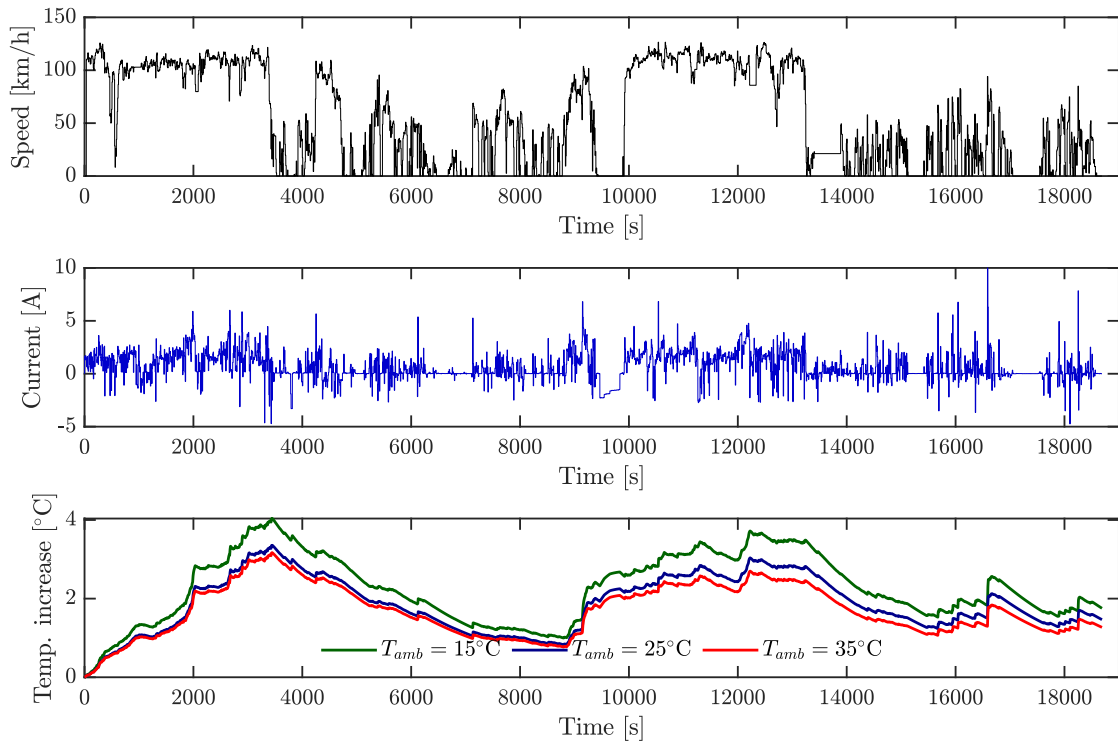


Figure 13. Battery temperature simulation under a real driving cycle. (**Top**) Velocity profile of a Nissan Leaf in a rural road with light traffic. (**Middle**) Scaled current. (**Bottom**) Temperature increase of the LCO 26650 LIB simulated at different ambient temperatures using the lumped model.

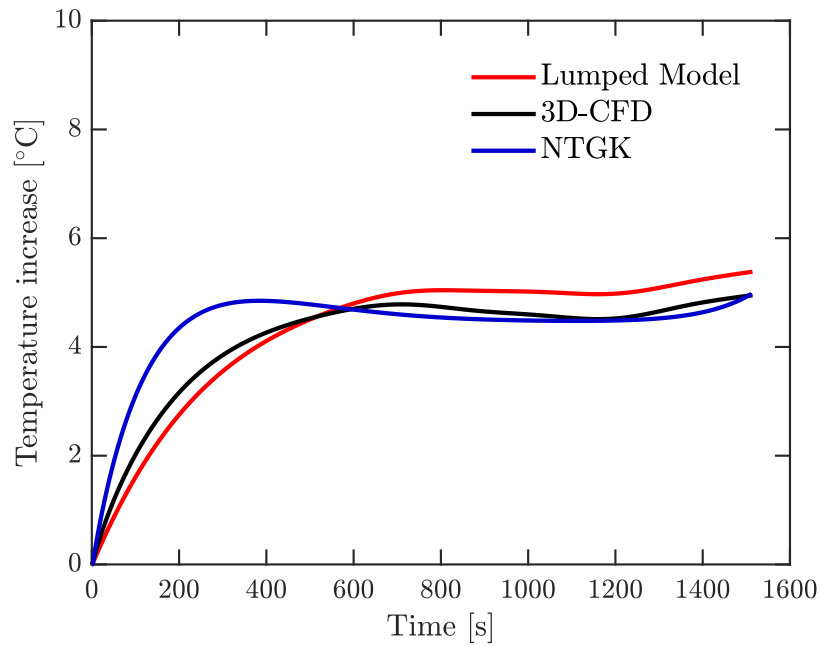


Figure 14. Comparison of methods for a simulated discharge at 2C under $h_{conv} = 100 \text{ W m}^{-2} \text{ K}^{-1}$.

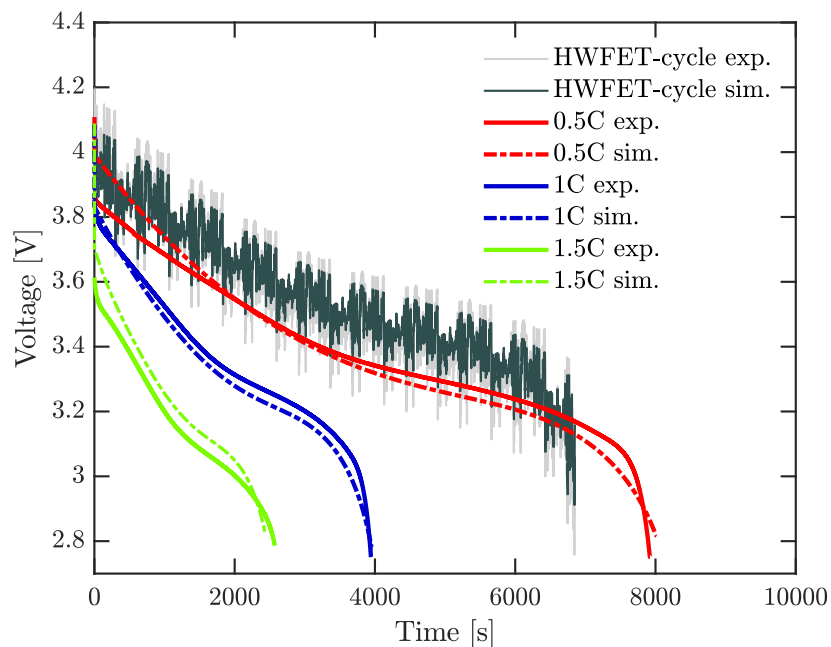


Figure 15. Comparison of experimental and simulated voltage using the NTGK model.

Computational Time

CPU time consuming is a relevant aspect while comparing among different proposed models in this work. All cases were run using a standard CPU (3.5 GHz, 16 GB RAM). As indicated in Table 13, the lumped model requires time in the order of seconds for solving the temperature profile. NTGK model is more time consuming since it has to evaluate many electrochemical equations in the battery domain, even under the consideration that its mesh has fewer number of elements with respect to 3D-CFD approach. Moreover, if a mesh with more number of elements is used, and if fluid flow around them is solved, the computational time will increase considerably.

Table 13. Execution time for the different models.

Current	Lumped	3D-CDF	NTGK
0.5C	2.03 s	1612 s	27120 s
1C	1.08 s	776 s	14280 s
1.5C	0.61 s	463 s	8989 s
HWFET-cycle	7.23 s	1296 s	26460 s

5. Conclusions

The temperature profile of a LCO 26650 lithium-ion battery under constant and complex current rates was evaluated by comparing three of the most used methods to study the thermal behavior of LIBs: a lumped model, 3D-CFD approach and an electrochemical method based on NTGK with dual potential approach. The heat generation rate, heat capacity, and heat transfer coefficients were estimated to predict the temperature at the cell surface. Thus, the following conclusions are drawn:

1. In general, NTGK model has the best performance over the rest of the studied models due to that it is capable to solve not only the temperature field of the cell, but also voltage, heat generation and other properties. This approach provides the lower temperature error at 0.5C. Nevertheless, this model presents the higher RMS error of 1.3 °C at 1.5C, where the maximum temperature increase of the cell was 18.1 °C. Under the driving cycle, the temperature increase was 5.1 °C, and all the models were in the same order of error.

2. Lumped model is suitable to use satisfactorily in a wide range of LIB operating conditions and it presents a very similar temperature profile as 3D formulation since both models depend on the same heat generation rate and thermal parameters.
3. Under free convection, radiation plays a relevant role in terms of heat transfer rate, this contribution is practically the same as convection. Besides, the heat transfer coefficient increases as the discharging current does.

Author Contributions: Conceptualization, E.P.-H. and W.R.C.-M.; methodology, W.R.C.-M., M.O. and K.M.; simulations, E.P.-H.; experiments, W.R.C.-M., M.O. and E.P.-H.; validation, W.R.C.-M., F.J. and M.O.; writing—original draft preparation, E.P.-H. and F.J. All the authors reviewed the paper. All authors have read and agreed to the published version of the manuscript.

Funding: This research was funded by SENESCYT Ecuador, and FONDECYT Chile grant number 1170044.

Acknowledgments: The authors would like to acknowledge to The Advanced Center for Electrical and Electronic Engineering, AC3E, Basal Project FB0008, ANID. Also, thanks to Mr. Jorge Reyes for his support in the laboratory.

Conflicts of Interest: The authors declare no conflict of interest. The funders had no role in the design of the study; in the collection, analyses, or interpretation of data; in the writing of the manuscript, or in the decision to publish the results.

Abbreviations

The following abbreviations are used in this manuscript:

Acronyms

1D	One-dimensional
2D	Two-dimensional
3D	Three-dimensional
BTMS	Battery thermal management system
C	Discharge rate
CC-CV	Constant-current constant-voltage
CFD	Computational fluid dynamics
DAQ	Data acquisition
DoD	Depth-of-discharge
ECM	Equivalent circuit model
EIS	Electrochemical impedance spectroscopy
EV	Electric vehicle
Exp.	Experiment
HPPC	Hybrid pulse power characterization
HWFET	The Highway Fuel Economy Test
LCO	Lithium cobalt oxide
LFP	Lithium iron phosphate
Li	Lithium
LIB	Lithium-ion battery
LiCoO ₂	Lithium cobalt oxide
MSMD	Multi-scale multi-domain
NTC	Negative temperature coefficient
NTGK	Newman, Tiedemann, Gu, and Kim
OCV	Open circuit voltage
RMS	Root mean square
RUL	Remaining useful life
SOC	State-of-charge

Constants and variables

\vec{V}	Velocity ($\text{m} \cdot \text{s}^{-1}$)
A	Area (m^2)
C_1	Temperature constant for a specific battery for NTGK model
C_2	Voltage constant for a specific battery for NTGK model
C_N	Nominal capacity of the battery (Ah)
C_p	Heat capacity (J K^{-1})
c_p	Specific heat capacity ($\text{J kg}^{-1} \text{K}^{-1}$)
C_{Nu}	Constant for Nusselt number
C_{ref}	Reference capacity of the cell (Ah)
d	Battery diameter (m)
E	Activation energy (J)
H	Enthalpy (J kg^{-1})
h	Heat transfer coefficient ($\text{W m}^{-2} \text{K}^{-1}$)
h_e	Sensible enthalpy (J kg^{-1})
I	Current (A)
j	Volumetric current (Am^{-3})
k_f	Thermal conductivity of the fluid ($\text{W m}^{-1} \text{K}^{-1}$)
k_c	Thermal conductivity of the cell ($\text{W m}^{-1} \text{K}^{-1}$)
m	Mass (kg)
Q	Heat transfer rate (W)
q_{ech}	Electrochemical heat (W)
Q_{ht}	Total heat transfer rate (W)
R_o	Ohmic resistance (Ω)
R_T	Total internal resistance (Ω)
R_{CT}	Charge transfer resistance (Ω)
R_{in}	Internal thermal resistance (K W^{-1})
R_{out}	External thermal resistance (K W^{-1})
S_h	Source term (W m^{-3})
T	Temperature (K)
t	Time (s)
U	Function for equilibrium potential for NTGK model
V	Voltage (V)
Vol	Volume of active zone (m^3)
Y	Function for NTGK model
Z	Impedance (Ω)
C	Rate of current discharge
Nu	Nusselt number
Ra	Rayleigh number

Greek Symbols

ϵ	Emissivity
∇	Divergence operator
ϕ	Potential (V)
ρ	Density (kg m^{-3})
σ	Steffan-Boltzmann constant $\sigma = 5.67 \times 10^{-8} \text{ W m}^{-2} \text{ K}^{-4}$, electrical conductivity (S/m)

Subscripts

<i>amb</i>	Ambient
<i>c</i>	Cell
<i>comb</i>	combined
<i>conv</i>	convection
<i>CT</i>	Charge transfer
<i>ech</i>	Electrochemical heat
<i>f</i>	Fluid
<i>ht</i>	Heat transfer
<i>in</i>	Internal
<i>N</i>	Nominal
<i>neg</i>	Relative to anode
<i>OC</i>	Open circuit
<i>out</i>	External
<i>pos</i>	Relative to cathode
<i>rad</i>	radiation
<i>ref</i>	Reference
<i>s</i>	Surface
<i>sur</i>	surround
<i>surf, c</i>	Cell surface
<i>T</i>	Total

Superscripts

<i>n</i>	Constant for Rayleigh number
°	Degree

References

1. Bryden, T.S.; Dimitrov, B.; Hilton, G.; Ponce de León, C.; Bugryniec, P.; Brown, S.; Cumming, D.; Cruden, A. Methodology to determine the heat capacity of lithium-ion cells. *J. Power Sources* **2018**, *395*, 369–378. [[CrossRef](#)]
2. Reyes-Mambrio, J.; Moser, F.; Gana, F.; Severino, B.; Calderón-Muñoz, W.R.; Palma-Behnke, R.; Estevez, P.A.; Orchard, M.; Cortés, M. A fractal time thermal model for predicting the surface temperature of air-cooled cylindrical Li-ion cells based on experimental measurements. *J. Power Sources* **2016**, *306*, 636–645. [[CrossRef](#)]
3. Forgez, C.; Vinh Do, D.; Friedrich, G.; Morcrette, M.; Delacourt, C. Thermal modeling of a cylindrical LiFePO₄/graphite lithium-ion battery. *J. Power Sources* **2010**, *195*, 2961–2968. [[CrossRef](#)]
4. Liu, X.; Ai, W.; Naylor Marlow, M.; Patel, Y.; Wu, B. The effect of cell-to-cell variations and thermal gradients on the performance and degradation of lithium-ion battery packs. *Appl. Energy* **2019**, *248*, 489–499. [[CrossRef](#)]
5. Coman, P.T.; Rayman, S.; White, R.E. A lumped model of venting during thermal runaway in a cylindrical lithium cobalt oxide lithium-ion cell. *J. Power Sources* **2016**, *307*, 56–62. [[CrossRef](#)]
6. Lin, X.; Perez, H.E.; Mohan, S.; Siegel, J.B.; Stefanopoulou, A.G.; Ding, Y.; Castanier, M.P. A lumped-parameter electro-thermal model for cylindrical batteries. *J. Power Sources* **2014**, *257*, 12–20. [[CrossRef](#)]
7. Gao, X.; Ma, Y.; Chen, H. Active thermal control of a battery pack under elevated temperatures. *IFAC-PapersOnLine* **2018**, *51*, 262–267. [[CrossRef](#)]
8. Patil, M.S.; Seo, J.H.; Panchal, S.; Jee, S.W.; Lee, M.Y. Investigation on thermal performance of water-cooled Li-ion pouch cell and pack at high discharge rate with U-turn type microchannel cold plate. *Int. J. Heat Mass Transf.* **2020**, *155*, 119728. [[CrossRef](#)]
9. Panchal, S.; Mathewson, S.; Fraser, R.; Culham, R.; Fowler, M. *Measurement of Temperature Gradient (dT/dy) and Temperature Response (dT/dt) of a Prismatic Lithium-Ion Pouch Cell with LiFePO₄ Cathode Material; WCX™ 17*: SAE World Congress Experience; SAE International: Detroit, MI, USA, 2017. [[CrossRef](#)]

10. Samba, A.; Omar, N.; Gualous, H.; Van den Bossche, P.; Van Mierlo, J.; Boubekeur, T.I. Development of 2D thermal battery model for Lithium-ion pouch cells. *World Electr. Veh. J.* **2013**, *6*, 629–637. [CrossRef]
11. Kim, Y.; Mohan, S.; Siegel, J.B.; Stefanopoulou, A.G.; Ding, Y. The estimation of temperature distribution in cylindrical battery cells under unknown cooling conditions. *IEEE Trans. Control Syst. Technol.* **2014**, *22*, 2277–2286. [CrossRef]
12. Richardson, R.R.; Zhao, S.; Howey, D.A. On-board monitoring of 2-D spatially-resolved temperatures in cylindrical lithium-ion batteries : Part I . Low-order thermal modelling. *J. Power Sources* **2016**, *326*, 377–388. [CrossRef]
13. Gümüşsu, E.; Ekici, Ö.; Köksal, M. 3-D CFD modeling and experimental testing of thermal behavior of a Li-Ion battery. *Appl. Therm. Eng.* **2017**, *120*, 484–495. [CrossRef]
14. Xia, Q.; Wang, Z.; Ren, Y.; Sun, B.; Yang, D.; Feng, Q. A reliability design method for a lithium-ion battery pack considering the thermal disequilibrium in electric vehicles. *J. Power Sources* **2018**, *386*, 10–20. [CrossRef]
15. Jiaqiang, E.; Yue, M.; Chen, J.; Zhu, H.; Deng, Y.; Zhu, Y.; Zhang, F.; Wen, M.; Zhang, B.; Kang, S. Effects of the different air cooling strategies on cooling performance of a lithium-ion battery module with baffle. *Appl. Therm. Eng.* **2018**, *144*, 231–241. [CrossRef]
16. Jilte, R.D.; Kumar, R. Numerical investigation on cooling performance of Li-ion battery thermal management system at high galvanostatic discharge. *Eng. Sci. Technol. Int. J.* **2018**, *21*, 957–969. [CrossRef]
17. Li, G.; Li, S. Physics-based CFD simulation of lithium-ion battery under the FUDS driving cycle. *ECS Trans.* **2015**, *64*, 1–14. [CrossRef]
18. Li, Y.; Zhou, Z.; Wu, W.T. Three-dimensional thermal modeling of Li-ion battery cell and 50 V Li-ion battery pack cooled by mini-channel cold plate. *Appl. Therm. Eng.* **2019**, *147*, 829–840. [CrossRef]
19. Panchal, S.; Mathew, M.; Fraser, R.; Fowler, M. Electrochemical thermal modeling and experimental measurements of 18650 cylindrical lithium-ion battery during discharge cycle for an EV. *Appl. Therm. Eng.* **2018**, *135*, 123–132. [CrossRef]
20. ANSYS Inc. *ANSYS Fluent Theory Guide (Release 18.0)*; ANSYS Inc.: Canonsburg, PA, USA, 2017.
21. Celik, A.; Coban, H.; Göçmen, S.; Ezan, M.; Goren, A.; Erek, A. Passive thermal management of the lithium-ion battery unit for a solar racing car. *Int. J. Energy Res.* **2019**, *43*, 3681–3691. [CrossRef]
22. Liu, Y.; Liao, Y.G.; Lai, M.C. Transient temperature distributions on lithium-Ion polymer SLI Battery. *Vehicles* **2019**, *1*, 127–137. [CrossRef]
23. Li, G.; Li, S.; Cao, J. Application of the MSMD framework in the simulation of battery packs. In Proceedings of the ASME 2014 International Mechanical Engineering Congress and Exposition, Volume 8B: Heat Transfer and Thermal Engineering, Montreal, QC, Canada, 14–20 November 2014; pp. 1–7. [CrossRef]
24. Madani, S.S.; Swierczynski, M.; Kær, S. Cooling Simulation and Thermal Abuse Modeling of Lithium-Ion Batteries Using the Newman, Tiedemann, Gu, and Kim (NTGK) Model. *ECS Trans.* **2017**, *81*, 261–270. [CrossRef]
25. Li, Q.; Yang, C.; Santhanagopalan, S.; Smith, K.; Lamb, J.; Steele, L.A.; Torres-Castro, L. Numerical investigation of thermal runaway mitigation through a passive thermal management system. *J. Power Sources* **2019**, *429*, 80–88. [CrossRef]
26. Hu, X.; Liu, W.; Lin, X.; Xie, Y. A Comparative Study of Control-Oriented Thermal Models for Cylindrical Li-Ion Batteries. *IEEE Trans. Transp. Electrif.* **2019**, *5*, 1237–1253. [CrossRef]
27. Bandhauer, T.M.; Garmella, S.; Fuller, T.F. A Critical Review of Thermal Issues in Lithium-Ion Batteries. *J. Electrochem. Soc.* **2011**, *158*, R1. [CrossRef]
28. Sun, J.; Wei, G.; Pei, L.; Lu, R.; Song, K.; Wu, C.; Zhu, C. Online internal temperature estimation for lithium-ion batteries based on Kalman filter. *Energies* **2015**, *8*, 4400–4415. [CrossRef]
29. Bergman, T.; Lavine, A. *Fundamentals of Heat and Mass Transfer*, 8th ed.; John Wiley & Sons, Inc.: Hoboken, NJ, USA, 2017; p. 1046.
30. Bernardi, D.; Pawlikowski, E.; Newman, J. A general energy balance for battery systems. *J. Electrochem. Soc.* **1985**, *132*, 5. [CrossRef]
31. Barai, A.; Chouchelamane, G.H.; Guo, Y.; Mcgordon, A.; Jennings, P. A study on the impact of lithium-ion cell relaxation on electrochemical impedance spectroscopy. *J. Power Sources* **2015**, *280*, 74–80. [CrossRef]
32. Stroe, D.I.; Swierczynski, M.; Stroe, A.I.; Knudsen Kær, S. Generalized Characterization Methodology for Performance Modelling of Lithium-Ion Batteries. *Batteries* **2016**, *2*, 37. [CrossRef]

33. Barai, A.; Uddin, K.; Widanage, W.D.; McGordon, A.; Jennings, P. A study of the influence of measurement timescale on internal resistance characterisation methodologies for lithium-ion cells. *Sci. Rep.* **2018**, *8*, 1–13. [[CrossRef](#)]
34. Pérez, A.; Benavides, M.; Rozas, H.; Seria, S.; Orchard, M. Guidelines for the characterization of the internal impedance of lithium-ion batteries in PHM algorithms. *Int. J. Progn. Health Manag.* **2018**, *9*, 1–10.
35. Waag, W.; Käbitz, S.; Sauer, D.U. Experimental investigation of the lithium-ion battery impedance characteristic at various conditions and aging states and its influence on the application. *Appl. Energy* **2013**, *102*, 885–897. [[CrossRef](#)]
36. Huang, J.; Li, Z.; Ge, H.; Zhang, J. Analytical solution to the impedance of electrode/electrolyte interface in lithium-ion batteries. *J. Electrochem. Soc.* **2015**, *162*, A7037–A7048. [[CrossRef](#)]
37. Kwon, K.H.; Shin, C.B.; Kang, T.H.; Kim, C.S. A two-dimensional modeling of a lithium-polymer battery. *J. Power Sources* **2006**, *163*, 151–157. [[CrossRef](#)]
38. Li, Q.; Yang, C.; Pesaran, A. *Thermal Runaway Propagation Modeling in Lithium Ion Modules with and without PCM*; Technical Report; International Battery Seminar & Exhibit: Fort Lauderdale, FL, USA, 2017.
39. Damay, N.; Forgez, C.; Bichat, M.P.; Friedrich, G. A method for the fast estimation of a battery entropy-variation high-resolution curve – Application on a commercial LiFePO₄/graphite cell. *J. Power Sources* **2016**, *332*, 149–153. [[CrossRef](#)]
40. Zhang, Y.; Song, W.; Feng, Z. An energy efficiency evaluation research based on heat generation behavior of lithium-ion battery. *J. Electrochem. Soc.* **2013**, *160*, 1927–1930. [[CrossRef](#)]
41. Kim, Y.; Siegel, J.B.; Stefanopoulou, A.G. A computationally efficient thermal model of cylindrical battery cells for the estimation of radially distributed temperatures. In Proceedings of the 2013 American Control Conference, Washington, DC, USA, 17–19 June 2013; pp. 698–703. [[CrossRef](#)]
42. Allafi, W.; Zhang, C.; Uddin, K.; Worwood, D.; Dinh, T.Q.; Ormeno, P.A.; Li, K.; Marco, J. A lumped thermal model of lithium-ion battery cells considering radiative heat transfer. *Appl. Therm. Eng.* **2018**, *143*, 472–481. [[CrossRef](#)]
43. Wang, Q.; Jiang, B.; Li, B.; Yan, Y. A critical review of thermal management models and solutions of lithium-ion batteries for the development of pure electric vehicles. *Renew. Sustain. Energy Rev.* **2016**, *64*, 106–128. [[CrossRef](#)]
44. Bahiraei, F.; Ghalkhani, M.; Fartaj, A.; Nazri, G.A. A pseudo 3D electrochemical-thermal modeling and analysis of a lithium-ion battery for electric vehicle thermal management applications. *Appl. Therm. Eng.* **2017**, *125*, 904–918. [[CrossRef](#)]
45. Madani, S.; Schaltz, E.; Knudsen Kær, S. Review of Parameter Determination for Thermal Modeling of Lithium Ion Batteries. *Batteries* **2018**, *4*, 20. [[CrossRef](#)]
46. Lin, X.; Stefanopoulou, A.; Siegel, J.; Mohan, S. Temperature Estimation in a Battery String Under Frugal Sensor Allocation. In Proceedings of the ASME 2014 Dynamic Systems and Control Conference, San Antonio, TX, USA, 22–24 October 2014; Volume 1. [[CrossRef](#)]
47. Calearo, L.; Thingvad, A.; Marinelli, M. Modeling of Battery Electric Vehicles for Degradation Studies. In Proceedings of the 2019 54th International Universities Power Engineering Conference (UPEC), Bucharest, Romania, 3–6 September 2019; pp. 1–6. [[CrossRef](#)]



© 2020 by the authors. Licensee MDPI, Basel, Switzerland. This article is an open access article distributed under the terms and conditions of the Creative Commons Attribution (CC BY) license (<http://creativecommons.org/licenses/by/4.0/>).